

# Radiation patterns in anisotropic models by Kirchhoff modelling/migration and AVO/AZ inversion

Hassan Khaniani and Daniel Trad

## ABSTRACT

We analyse the framework of Full Waveform Inversion (FWI) methods for multiparameter inversion of precritical reflection data in 3D model. We coupled the Kirchhoff based forward modeling, migration and inversion for inversion of P-to-P data acquired from 3D anisotropic media. The AVO/AZ approximation of weak contrast anisotropic models and Double Square Root (DSR) equation for traveltime consideration of P-to-P are implemented during inversion. The uncertainty of the procedure is analytically and numerically tested on a synthetic data that acquired from different acquisition patterns.

## INTRODUCTION

In exploration seismology, a method of subsurface parameter estimation is commonly referred as Full Waveform Inversion (FWI). The approach is usually iterative least squares problem (see e.g., Gauthier et. al., 1986, Virieux and Operto, 2009) based on perturbation theory (e.g., Morse and Feshbach, 1953, Cohen and Bleistein, 1987, Beylkin, 1990 and Moradi and Innanen, 2015) to relate the perturbation in model parameters to the data residual. The data residual is the difference between the modeled data and the true data. For inversion, an initial model close to the true model is chosen to migrate the data residual. The data residual is used for estimation of the gradient functions. The initial model is updated by gradient functions by a misfit criteria that the data residual is small enough. Therefore, the main steps in FWI algorithms are the forward modeling, migration and inversion.

For many reservoir scale seismic data studies, the subsurface structures are not too complex and the Kirchhoff approximation works well for wavefield modeling and imaging (Khaniani et. al., 2012). In this study, we assume that the data contains only primary pre-critical P-to-P reflection waves (i.e., multiples free). We use the Kirchhoff approximation to analyse the Full Waveform Inversion (FWI) result of a 3D reflection dataset. The waveform characteristic in terms of traveltime and amplitude are approximated by the Double Square Root (DSR) equation and the linearized Amplitude Variation with Offset method (AVO) (Rüger, 1997). This approach considers pre-critical reflection data for modeling and inversion. For the horizontal axis of symmetry, i.e. horizontal transverse isotropy (HTI) media, the azimuthal dependant amplitude variation with azimuth (AVO/AZ) is used, while for analysis of the vertical axis of symmetry, i.e. vertical transverse isotropy (VTI) media, amplitude variation with offset (AVO) is used.

Although much research has been performed to develop faster algorithms for the FWI application, this particular work is among the earliest attempts to expedite the FWI process by using Kirchhoff modeling and migration for 3D problems (Khaniani et al, 2015). The gradient function is obtained by sensitivity of classical AVO/AVAZ approaches to subsurface isotropic and anisotropic properties. A reference data is created

using an initial model and known azimuth of symmetry axes. The azimuth of symmetry axis is inverted by angular rotation of the migrated reference data with respect to the scatterpoint. The optimum axis of symmetry is obtained by least squares of the residual of the rotated and true migrated slices. After obtaining the azimuth of symmetry axis, we can use AVO/AZ attribute analysis for inversion.

By comparing the analytical solution of anisotropic reflectivity and numerical result of 3D Kirchhoff based modeling and migration over different acquisition parameters, we analyze the performance of AVO/AZ inversion in a 3D medium. By describing the numerical aspects of FWI by pre-stack time migration (PSTM) and AVO/AVAZ, we hope to provide a tool that other scientists can use to visualize the radiation patterns of an isotropic and anisotropic media. The FWI framework is applied here only to synthetic data, but application to real seismic reflection data is left for future research.

## THEORY

### General nonlinear inverse problem

Suppose that the data,  $d_{true}$ , is predicted by a forward modeling operator,  $f$ , and that the true model parameter,  $m_{true}$ , is given by

$$f(m_{true}) = d_{true}, \quad (1)$$

The point of a generalized nonlinear inverse problem is to find a pair of  $d$  and  $m$  such that they have the closest distance to the pair of  $d_{true}$  and  $m_{true}$ . To solve equation (1) using the least square optimization approach, a misfit function,  $J$ , is used:

$$J = \frac{1}{2} \|\delta d_k\|^2 + \frac{1}{2} \|\delta m_k\|^2. \quad (2)$$

The symbol,  $\|\cdot\|$ , is the norm,  $\delta d_k = d_{true} - d_k$  and the subscript  $k$  represents the iteration number. From equation (2), the model parameter can be updated by

$$m_{k+1} = m_k + \delta m_k, \quad (3)$$

where,  $\delta m_k$  is the model perturbation obtained by minimization of  $J$ ,

$$\delta m_k = - \left[ \frac{\partial^2 J(m_k)}{\partial m_k^2} \right]^{-1} \frac{\partial J(m_k)}{\partial m_k}. \quad (4)$$

The gradient function  $\frac{\partial J(m)}{\partial m}$  is given by (Tarantola, 1984)

$$\gamma = \frac{\partial J(m)}{\partial m} = -[F^* \delta d], \quad (5)$$

where  $F^*$  is the transpose of a linear operator defined as the derivative of  $f$  at the point  $m$  with the elements of a model with dimension of  $N \times M$  given by

$$F_{ij} = \frac{\partial f_i}{\partial m_j}, \quad i = (1, \dots, N), \quad j = (1, \dots, M). \quad (6)$$

In this study,  $F^*$  is called the numerical operator for migration/inversion to be designed by a set of appropriate imaging and inversion operators to produce the gradient function,  $\gamma$ . The gradient function describes the sensitivity of waveform information to isotropic and anisotropic parameters. We analyze the radiation pattern of scatterpoints for estimation of gradient function. Therefore, the multiparameters gradient functions are obtained by AVO/AZ analysis. The operator,  $\frac{\partial^2 J(m)}{\partial m^2}$ , is called the Hessian and is assumed to be a scalar coefficient here. So, equation (4) reduces to

$$\delta m_k \approx -\alpha \gamma_k, \quad (7)$$

where  $\alpha$  is called the step length at each iteration and the updating procedure is done by using the steepest decent method. Khaniani et al., (2015) show a general framework of the iterative inversion using a 2D isotropic elastic Kirchhoff approximation. The traveltimes of the operator,  $f$  and  $F^*$ , are based on the DSR equation, which in seismic problems is referred to as the Prestack Time modeling/migration (PSTM). The amplitude character of the seismic waveform is based on the AVO/AZ operator.

To analyse the gradient function, we discuss the performance of AVO/AZ inversion using numerical modeling, migration and inversion on isotropic and anisotropic parameters.

### Forward problem

For high frequency approximations, the single scattered wavefield components of the elastic waves can be expressed as (Beylkin and Burridge, 1990)

$$\delta d_{jk}^{IR} = -\partial_t \int S_{lm}^{IR} A_{jl}^I A_{km}^R \delta(t - \phi^I - \phi^R) d\mathbf{x}, \quad (8)$$

where,  $S_{lm}^{IR}$  is the scattering matrix, superscripts  $I$  and  $R$  refer to incident and reflected waves, the subscripts  $jk$  indicate the displacement in the  $k$ -direction due to a point force in the  $j$ -direction. The terms  $A^I$  and  $A^R$  are true amplitude factors,  $\phi^I$  and  $\phi^R$  are the traveltimes for the incident and reflected waves respectively. In the contrast model, the scattering operator in equation (8) can be expressed by the Kirchhoff approximation as (Beylkin and Burridge, 1990, Jaramillo and Bleistein, 1999, Shaw and Sen, 2004 and Kroode, 2012):

$$S(\mathbf{x}) = \left[ (\delta\rho^+(\mathbf{x}) - \delta\rho^-(\mathbf{x})) \delta_{ik} + (\delta c_{ijkl}^+(\mathbf{x}) - \delta c_{ijkl}^-(\mathbf{x})) p_j^R p_l^I \right] h_k^I h_i^R .. \quad (9)$$

The (+/-) superscripts refer to the upper/lower media, the  $p$  is the slowness vector and  $h$  is the polarization unit vector. We can see that the radiation pattern varies with changes in density and stiffness tensor across the reflection boundary. Generally, in anisotropic medium, properties of  $c_{ijkl}$  and the angle dependent variations of  $p$  and  $h$  give an additional term to anisotropic reflectivity functions. The weak-contrast linearized reflection coefficients  $R(x)$  (Aki and Richards, 1980) and the Kirchhoff scattering

potential in equation (9) are related by (Ursin and Tygel, 1997 and Shaw and Sen, 2004) through the following equation,

$$R(x) = -S(x) \frac{(\tan \theta^I + \tan \theta^R)^{1/2}}{2 \sin(\theta^I + \theta^R)}, \quad (10)$$

where,  $\theta^I$  and  $\theta^R$  are the angle of incident and reflected waves respectively. Figure 1a shows an HTI model where, the axis of symmetry is perpendicular to the anisotropic surface (Horizontal x2 axis). The reflectivity function in a HTI medium is angle and azimuth dependent and is given by,

$$R_P^{HTI}(\theta, \phi) = A^{iso} \frac{\Delta v_p}{\bar{v}_p} + B^{iso} \frac{\Delta Z}{\bar{Z}} + C^{iso} \frac{\Delta G}{\bar{G}} + D^{HTI} \Delta \delta^{(V)} + E^{HTI} \Delta \epsilon^{(V)} + F^{HTI} \Delta \gamma, \quad (11)$$

where,  $\theta$  denotes the incident phase angle as shown in Figure 1,  $Z = \rho v_p$  is P-wave impedance,  $\rho$  is density and  $G = \rho v_s^2$  is S-wave impedance. The operator  $\Delta$  is the differential operator on the bedding boundaries. The P-wave and S-wave velocities,  $v_p$  and  $v_s$ , and the anisotropic parameters are defined with the following relationships:

$$v_p = \sqrt{c_{33} / \rho}, \quad (12)$$

$$v_s = \sqrt{c_{55} / \rho} \quad (13)$$

$$\gamma = \frac{c_{66} - c_{55}}{2c_{55}}, \quad (14)$$

$$\epsilon = \frac{c_{11} - c_{33}}{2c_{33}}, \quad (15)$$

and

$$\delta = \frac{(c_{13} + c_{55})^2 - (c_{33} - c_{55})^2}{2c_{33}(c_{33} - c_{55})}, \quad (16)$$

where,  $c_{ij}$  are the components of the stiffness tensor in Voigt notation. The stiffness tensors for HTI and VTI medium are different because of different direction of symmetry axes as defined by (Musgrave, 1970 and Rüger, 2001)

$$c^{HTI} = \begin{pmatrix} c_{11} & c_{13} & c_{13} & & & \\ c_{13} & c_{33} & (c_{33} - 2c_{44}) & & & \\ c_{13} & (c_{33} - 2c_{44}) & c_{33} & & & \\ & & & c_{44} & & \\ & & & & c_{55} & \\ & & & & & c_{55} \end{pmatrix} \quad (17)$$

and

$$c^{VTI} = \begin{pmatrix} c_{11} & (c_{11} - 2c_{66}) & c_{13} & & & \\ (c_{11} - 2c_{66}) & c_{11} & c_{13} & & & \\ c_{13} & c_{13} & c_{33} & & & \\ & & & c_{55} & & \\ & & & & c_{55} & \\ & & & & & c_{66} \end{pmatrix}. \quad (18)$$

The parameter  $\gamma$  denotes the fractional difference between the horizontal and vertical SH-wave velocity,  $\varepsilon$  denotes the fractional difference between horizontal and vertical P-wave velocity, and  $\delta$  describes the variation of P-wave velocity with phase angle for near vertical velocity (Rüger, 2001). The coefficients are defined by,

$$\begin{aligned} A^{iso} &= \frac{1}{2} \tan^2 \theta, \\ B^{iso} &= \frac{1}{2}, \\ C^{iso} &= -\frac{1}{2} \left( 2 \frac{\bar{v}_S}{\bar{v}_P} \right)^2 \sin^2 \theta, \\ D^{HTI} &= \frac{1}{2} (1 + \sin^2 \phi \tan^2 \theta) \cos^2 \phi \sin^2 \theta \\ E^{HTI} &= \frac{1}{2} \cos^4 \phi \sin^2 \theta \tan^2 \theta \\ F^{HTI} &= \frac{1}{2} \left( 2 \frac{\bar{v}_S}{\bar{v}_P} \right)^2 \cos^2 \phi \sin^2 \theta \end{aligned} \quad (19)$$

The P-P reflectivity function for an anisotropic VTI medium is given by (Rüger, 1997)

$$R_P^{VTI}(\theta, \phi) = A^{iso} \frac{\Delta v_p}{\bar{v}_p} + B^{iso} \frac{\Delta Z}{\bar{Z}} + C^{iso} \frac{\Delta G}{\bar{G}} + D \Delta \delta^{(V)} + E \Delta \varepsilon^{(V)} + F \Delta \gamma, \quad (20)$$

where, the coefficients are defined by,

$$\begin{aligned}
 D^{VTI} &= \frac{1}{2} \sin^2 \theta, \\
 E^{VTI} &= \frac{1}{2} \sin^2 \theta \tan^2 \theta, \\
 F^{VTI} &= 0.
 \end{aligned} \tag{21}$$

Using the assumption of weak anisotropy, the phase velocity of P-wave propagating in HTI can be linearized in terms of  $\theta$ ,  $\phi$ ,  $\varepsilon$  and  $\delta$  (Tsvankin, 1997a)

$$v_P^{HTI}(\theta, \phi) = v_{P0} \left[ 1 + \varepsilon^{(V)} \cos^4 \phi \sin^4 \phi + \delta^{(V)} \cos^2 \phi \sin^2 \theta (\cos^2 \theta + \sin^2 \phi \sin^2 \theta) \right], \tag{22}$$

where,  $v_{P0}$  is the P-wave velocity in isotropic media. The angle dependent phase velocity of P-wave propagating in VTI can be expressed in terms of  $\theta$ ,  $\varepsilon$  and  $\delta$  (Tsvankin, 1997 and Tsvankin, 1997b)

$$v_P^{VTI}(\theta) = v_{P0} \left[ 1 + \varepsilon^{(V)} \sin^4 \theta + \delta^{(V)} \sin^2 \theta \cos^2 \theta \right]. \tag{23}$$

The variation of anisotropic P-wave velocity in HTI and VTI medium are compared in Figure 2. The azimuth  $\phi$  are referenced with respect to the x-axis direction (see Figure 1b), and the incident angle  $\theta$  is estimated with respect to the target layer at a depth of 500 m and isotropic velocity  $v_{P0} = 2500$  m/s. As shown in Figure 2a, the distribution of velocity is symmetric with respect to the anisotropic symmetry axis while in VTI media its variation depends on the angle of incident. Studies of the traveltimes of seismic events due to the effects of anisotropic parameters are useful for tomography (e.g. Grésillaud & Cara 1996). The objective of this study is to investigate the radiation pattern of VTI and HTI medium and the role of acquisition parameters for AVO/AZ inversion. Hence, we ignore the effects of anisotropy in traveltimes but we take them into account for amplitude variations. We do this by considering the velocity of isotropic models for traveltime calculations.

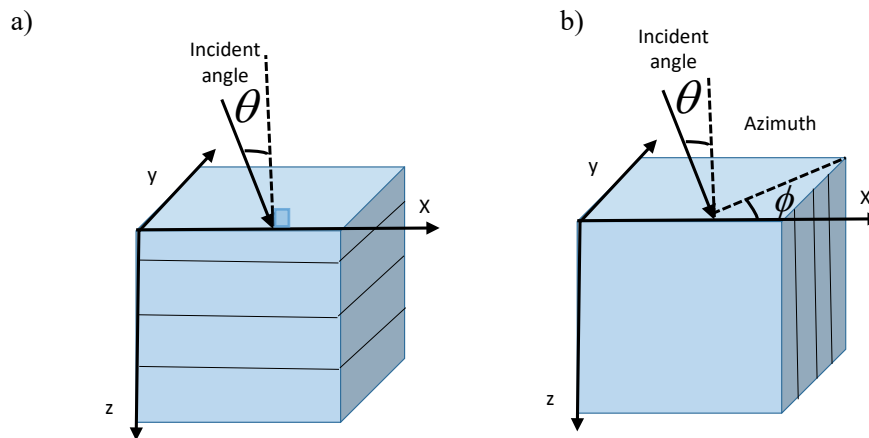


Figure 1: The schematic of anisotropic model for a) the VTI medium and b) the HTI medium. The incident angle  $\theta$  is defined with respect to the normal vector of x-y plane while the azimuth  $\phi$  is defined with respect to an arbitrary direction (e.g., x- direction) within the x-y plane.

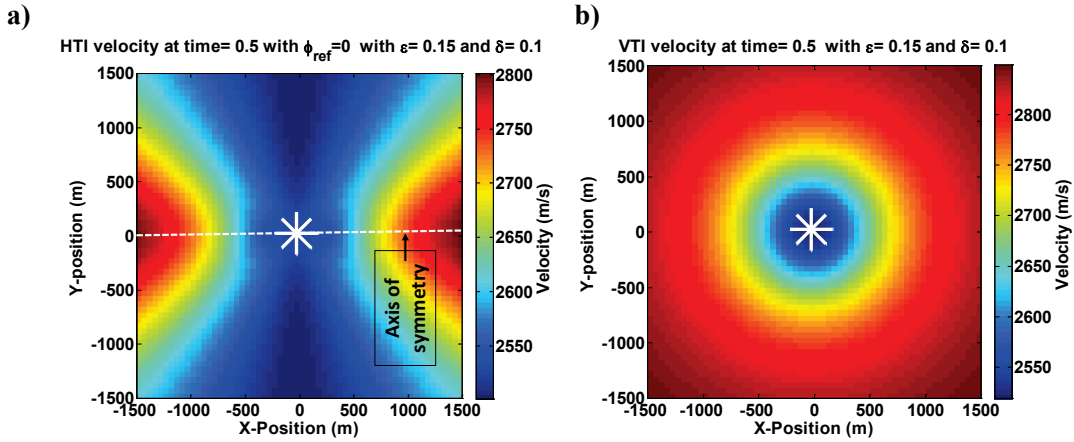


Figure 2: P-wave velocity variation for a) HTI and b) VTI medium. The evaluation is based on a target layer at 500 m depth propagating in the anisotropic medium with  $\varepsilon = 0.15$ ,  $\delta = 0.1$  and the isotropic velocity  $v_{P0} = 2500$  m/s.

### Inversion for azimuth angle of symmetry $\phi_{ref}$

The angle/azimuth dependent reflectivity function of an earth model is shown in Figure 3. The HTI models are evaluated using equation (11), with the input parameters listed in Table 1. The reference azimuth is based on  $x$  direction as shown in Figure 1b. The angles of incidence are estimated based on the distance from the source in the center of the model. The model lengths in x and y directions are 3 by 3 km, and the target layer is at a depth of 500 m. The grid size of the model in x and y dimensions are arbitrarily chosen to be  $Dx_1 = Dx_2 = 100$  m.

For inversion, the radiation patterns of different HTI and VTI model parameters are analytically estimated and mapped to scatter point positions. The terms in  $A^{iso}$ ,  $B^{iso}$  and  $C^{iso}$  make contribution to the reflectivity of the isotropic model in (11). These terms are not dependent on the azimuth of the axis of symmetry  $\phi$ . In the isotropic scenario in Figure 3a, the distribution of angle dependent reflectivity functions has a circular pattern. In contrast with isotropic model, the radiation pattern HTI scenarios, are influenced by both  $\theta$  and  $\phi$ . Figure 3b shows the radiation pattern of HTI#1 scenario which are listed in Table 1. It shows that the estimated radiation patterns are symmetric around the azimuth of the axis of symmetry which is  $\phi_{ref} = 0$ . Similarly, the axis of symmetry of 45° and 90° in the HTI#2 and HTI#3 scenarios are evaluated in Figure 3 (c and d), which shows their radiation patterns rotated with respect to the axis of symmetry. We use this important property to estimate the azimuth of the axis of symmetry, by performing the following steps:

- I. For an anisotropic model, perform 3D modeling by assuming a reference azimuth.
- II. Perform migration of the modeled data.

- III. Extract a time (or depth) slice corresponding to a target layer and rotate the migration result with respect to the scatter point position and
- IV. perform the cross-correlation of the rotated image and find the optimum  $\phi_{ref}$ .

For a flat reflector, we can consider the radiation pattern of a single shot position to be like the radiation pattern of a single scatter point. Thus, we analyze a single shot record to resemble a Common Image Gather (CIG) of a single scatter point.

To demonstrate the radiation patterns of anisotropic parameters  $\delta^{(V)}$ ,  $\varepsilon^{(V)}$  and  $\gamma$ , three models HTI#4, HTI#5 and HTI#6 are evaluated with azimuth  $\phi_{ref} = 0$ . The relative change of velocities  $v_p$  and P-wave impedance  $Z$  and shear modulus  $G$  are assumed to be negligible, i.e.,  $\Delta v_p / \bar{v}_p = 0$ ,  $\Delta Z / \bar{Z} = 0$  and  $\Delta G / \bar{G} = 0$ . Figure 4 shows that the radiation with different anisotropic parameters has different patterns. According to Rüger (1997), the analysis of these radiation patterns provides an intuitive attribute for estimation of anisotropic parameters of subsurface.

Table 1: Model parameters used for evaluation of AVO/AZ reflection coefficient.

Modeling	$\frac{\Delta v_p}{\bar{v}_p}$	$\frac{\Delta Z}{\bar{Z}}$	$\frac{\Delta G}{\bar{G}}$	$\Delta \delta^{(V)}$	$\Delta \varepsilon^{(V)}$	$\Delta \gamma$	$\phi_{ref}^o$
Isotropic	0.1	0.1	0.1	0	0	0	NA
HTI #1	0.1	0.1	0.1	0.1	0.1	0.1	0°
HTI #2	0.1	0.1	0.1	0.1	0.1	0.1	45°
HTI #3	0.1	0.1	0.1	0.1	0.1	0.1	90°
HTI #4	0.0	0.0	0.0	0.1	0.0	0.0	0°
HTI #5	0.0	0.0	0.0	0.0	0.1	0.0	0°
HTI #6	0.0	0.0	0.0	0.0	0.0	0.1	0°
VTI #1	0.0	0.0	0.0	0.1	0.0	NA	NA
VTI #2	0.0	0.0	0.0	0.0	0.1	NA	NA

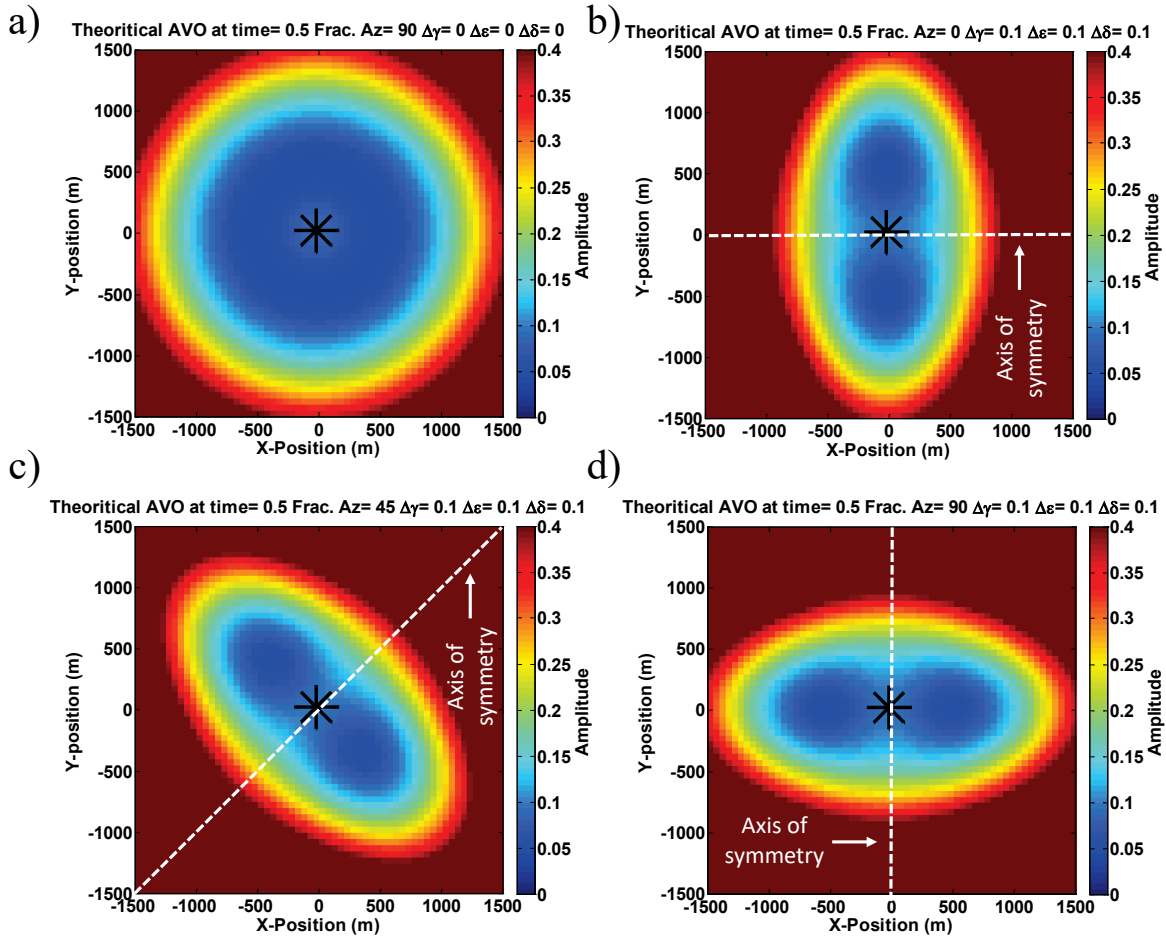


Figure 3: Evaluation of AVO/AZ formulation Rüger (1997) for different azimuth of axis of symmetry. a) Isotropic media, b) HTI#1 media with axis of symmetry of  $\phi_{ref} = 0$ , c) HTI#2 media with axis of symmetry of  $\phi_{ref} = 45$  and d) HTI #3 media with axis of symmetry of  $\phi_{ref} = 90$ . The star label in middle represents the source position.

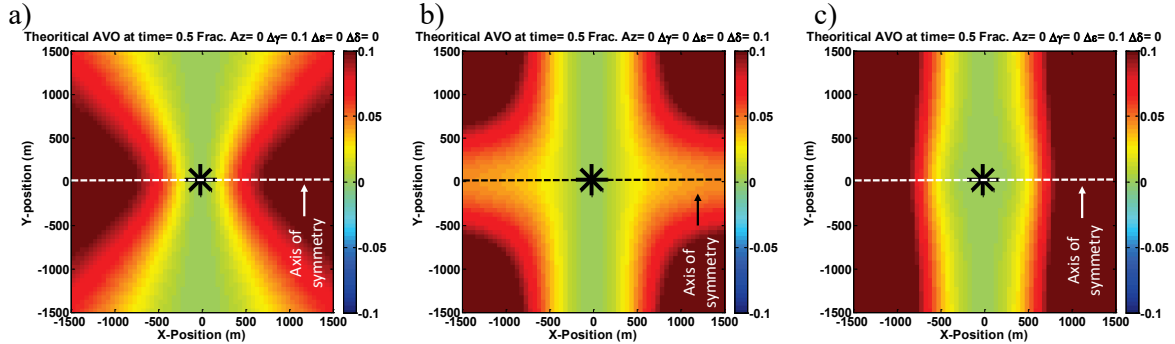


Figure 4: Evaluation of radiation pattern of anisotropic parameters for HTI media having  $\phi_{ref} = 0$ . a) Radiation pattern of  $\Delta\gamma$  in HTI#4 scenario, b) the radiation pattern of  $\Delta\delta$  in HTI#5 scenario and c) Radiation pattern of  $\Delta\epsilon$  in HTI#6 scenario.

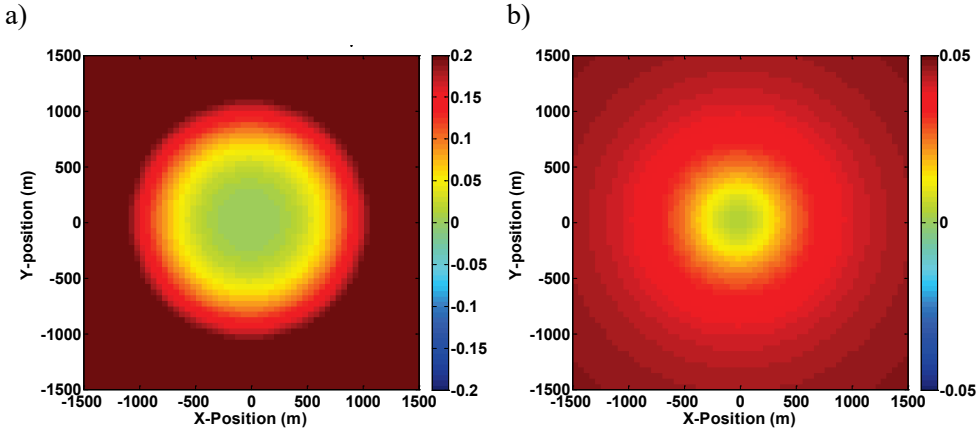


Figure 5: Evaluation of radiation pattern of anisotropic parameters for VTI media. a) Radiation pattern of  $\Delta\epsilon$  in VTI#1 scenario, b) the radiation pattern of  $\Delta\delta$  in VTI#2 scenario.

## NUMERICAL IMPLEMENTATION

### 2D isotropic modeling

In this section, we use equation (8) and AVO/AZ equation of (11) for simulation HTI medium and equation (20) for simulation of VTI medium. To demonstrate the efficiency of Kirchhoff modeling, we first perform a 2D isotropic modeling of field data set. We chose 51 shot records that were acquired by Nexen Energy ULC in NEBC. The receiver spacing is 10 m and the source spacing is 60 m. The source type was Vibroseis with vertical vibration mode. The sample rate is 4 ms and the grid lateral spacing for the modeling is 12.5 m. The well log in Figure 6 is used for input parameter of the forward modeling operator. Figure 7 shows a sample of the vertical component recorded data. The data of post critical angles are muted. As shown the main features of these modeled data are consistent with the field data set. The use of PSTM for P-P data is a current standard approach for imaging and is skipped here.

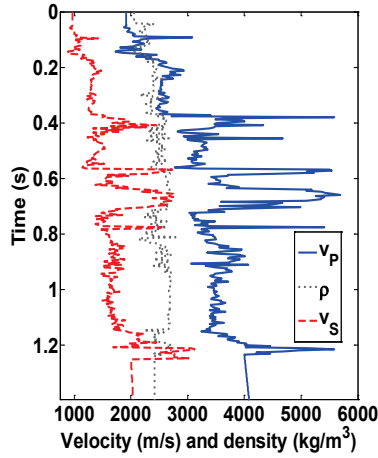


Figure 6: The well log data used for forward modeling.

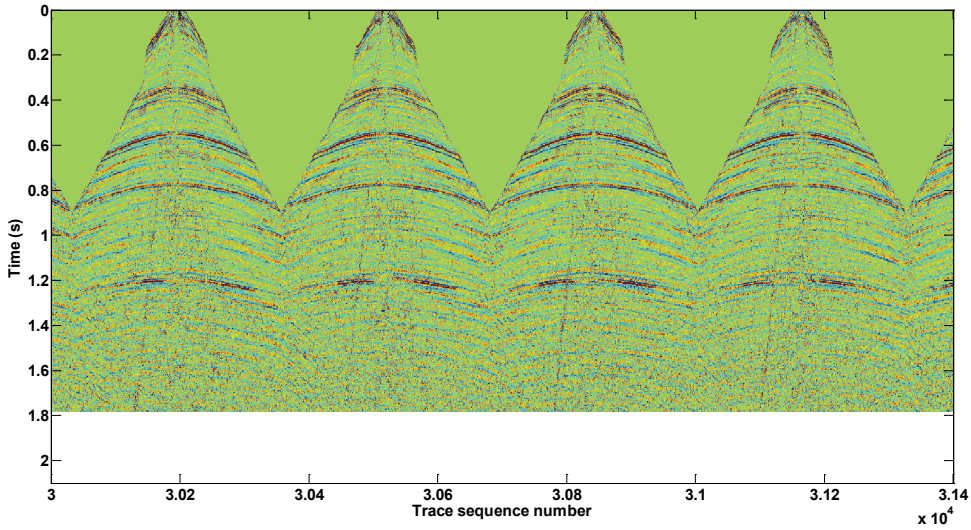


Figure 7: Arbitrary trace of 2D field data. Data obtained from Nexen Energy ULC in NEBC.

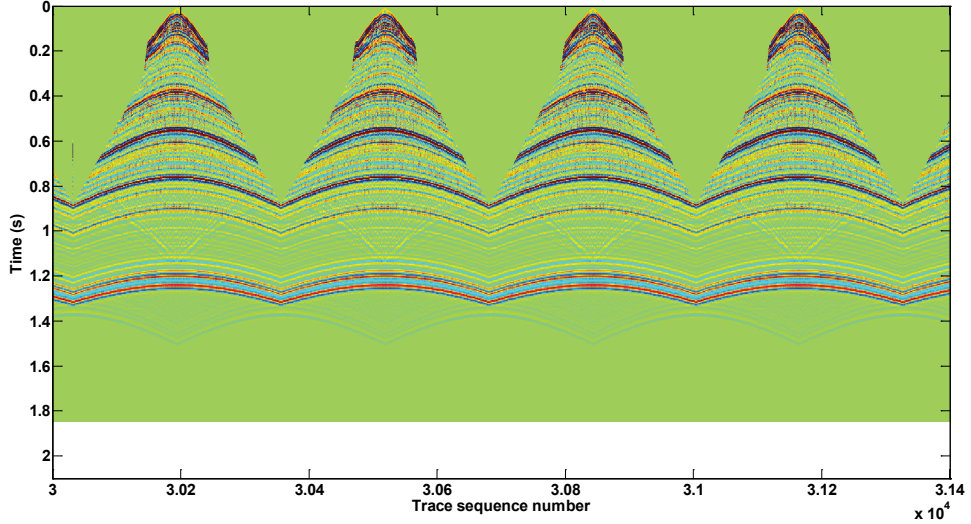


Figure 8: Arbitrary trace of 2D modeled data in Figure 7.

### 3D anisotropic modeling

In this section, we evaluate the results of Kirchhoff based forward modeling and migration for two 3D acquisition parameters in Table 2. The dimension of the model and the depth of the target is the same as in Figure 3. The model anisotropic parameters of Table 1 are chosen for modeling. Here, as shown in Table 2, we have changed the receiver spacing,  $dx_{rec}$  and  $dy_{rec}$ , and the subsurface bin size  $dx_{bin}$  for modeling and migration. The modeled shot records are shown in Figure 9 to Figure 12. As seen in the shot records, because of different radiation patterns of the simulated models, the waveform amplitudes of the receivers have different patterns. The numerical artefacts in these figures are due to the amplitude of diffraction from boundary.

Table 2: Acquisition and migration parameter used for 3D survey

	Length in $x$	Length in $y$	Length in $t$	$dx_{bin}$	$dy_{bin}$	$dx_{rec}$	$dy_{rec}$
Modeling #2	3000 m	3000 m	1.5 s	50 m	50 m	100 m	100 m
Migration#2	3000 m	3000 m	0.5 s	50 m	50 m	100 m	100 m
Modeling #1	3000 m	3000 m	1.5 s	50 m	50 m	25 m	375 m
Migration#1	3000 m	3000 m	0.5 s	12.5 m	12.5 m	25 m	375 m

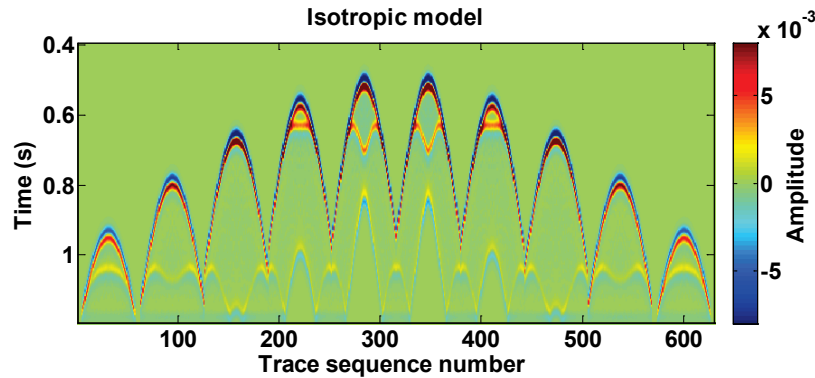


Figure 9: 3D modeled data. The Modeling#1 and isotropic parameters of Table 1 is used for modeling.

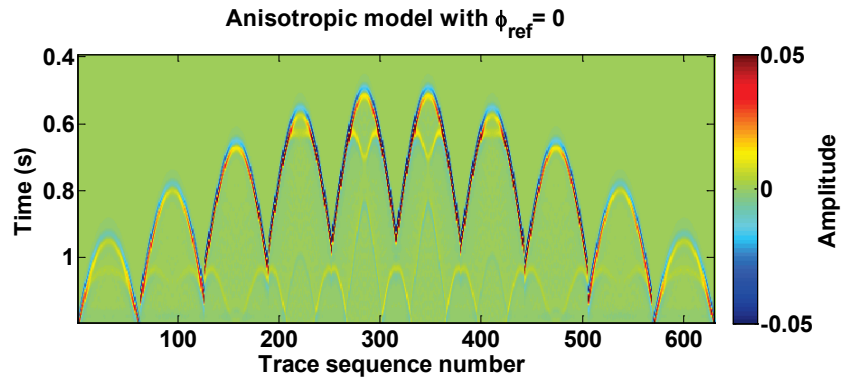


Figure 10: 3D modeled data. The Modeling#1 and HTI#1 parameters of Table 1 is used for modeling.

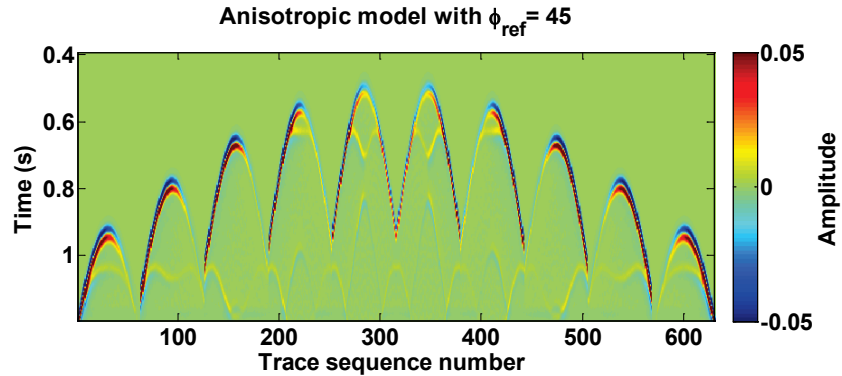


Figure 11: 3D modeled data. The Modeling#1 and HTI#2 parameters of Table 1 is used for modeling.

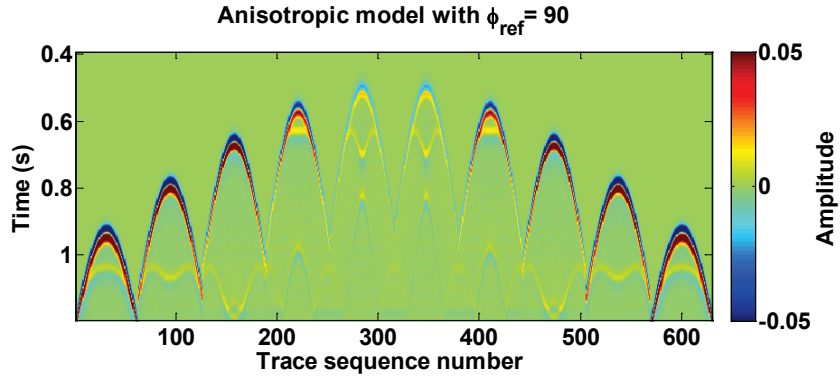


Figure 12: 3D modeled data. The Modeling#1 and HTI#3 parameters of Table 1 is used for modeling.

### Migration and Inversion

To analyse anisotropic radiation patterns, we migrate the shot record with 3D PSTM. We used small migration bin size to compensate for poor sampling artefacts as shown in table 1. The time slice of the target zone is shown in Figure 13. Still the acquisition artefacts are visible in migration results. Fortunately, the radiation patterns are recognisable for AVO analysis. In Figure 14, the amplitudes of a time slice of isotropic scenarios are compared for five azimuths, which are sampled along the black lines, namely AB, AC, AD, AE, AF, with azimuths of  $0^\circ$ ,  $30^\circ$ ,  $45^\circ$ ,  $60^\circ$  and  $90^\circ$  respectively. As expected, the sampling of different azimuths of isotropic models show similar trend, which can be used as a tool for AVO attributes. In Figure 16b to Figure 16d, similar analysis is performed for anisotropic model scenarios. Comparing the AVO/AZ curves of  $\phi_{ref} = 45$  (see Figure 14c) shows that the curves of  $\phi = 0$  and  $\phi = 90$  have similar trend. The curves of  $\phi_{ref} = 0$  (see Figure 14b) and  $\phi_{ref} = 90$  (see Figure 14b) have similar trends of AVO/AZ curves. However, the slight difference in amplitude values are due to the acquisition restrictions.

In Figure 16, the acquisition geometry of receivers changed according to Modeling/Migration#2 scenario listed in Table 2. Because of the even space sampling of the waveform, the radiation of the migration result are more consistent with the results of theoretical evaluations. Like the scenario of Modeling/Migration#1, the AVO/AZ curves are produced for five azimuths sampled along the black lines, namely AB, AC, AD, AE, AF. As seen in Figure 17, the symmetric behavior of the radiation pattern with respect to axis of anisotropic and more balanced amplitude of the AVO/AZ curves show that AVO/AZ curves are more stable compared to scenario of Modeling/Migration#1.

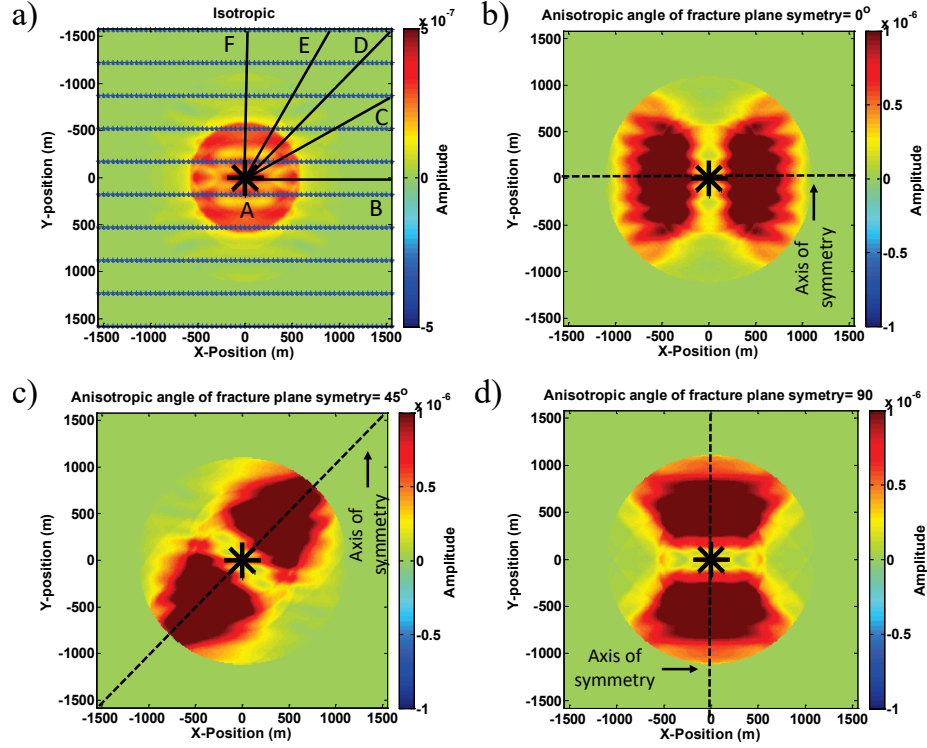


Figure 13: Evaluation of AVO/AZ formulation for different azimuth of axis of symmetry. The scenarios of Modeling#1 and Migration#1 are implemented for a) isotropic media, b) HTI #1 media with axis of symmetry of  $\phi_{ref} = 0^\circ$ , c) HTI#2 media with axis of symmetry of  $\phi_{ref} = 45^\circ$  and d) HTI #3 media with axis of symmetry of  $\phi_{ref} = 90^\circ$ . The solid line in a) correspond to AVO/AZ curves sampling along AB, AC, AD, AE and AF which have azimuth of  $0^\circ, 30^\circ, 45^\circ, 60^\circ$  and  $90^\circ$  respectively.

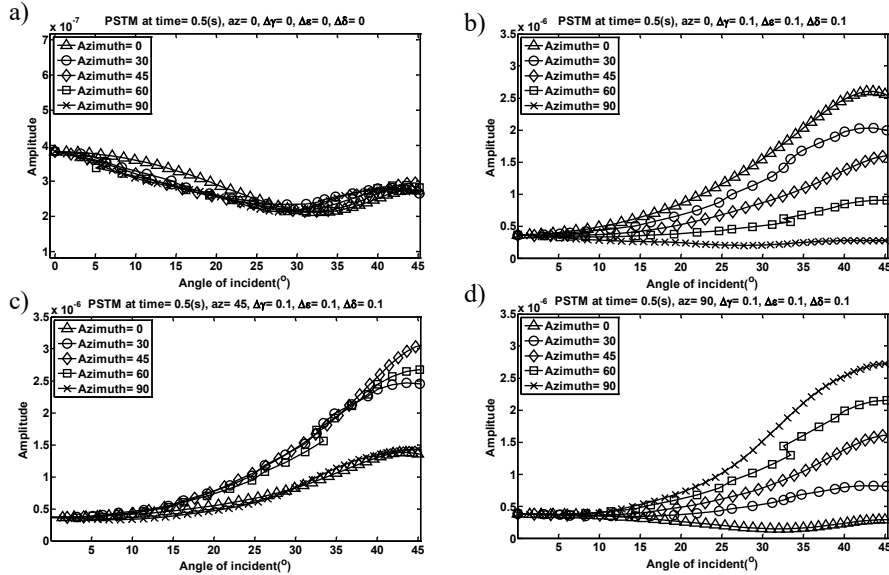


Figure 14: The AVO/AZ curves sampled from Figure 15. The scenarios for a) isotropic media, b) HTI #1 media with axis of symmetry of  $\phi_{ref} = 0^\circ$ , c) HTI#2 media with axis of symmetry of  $\phi_{ref} = 45^\circ$  and d) HTI #3 media with axis of symmetry of  $\phi_{ref} = 90^\circ$ .

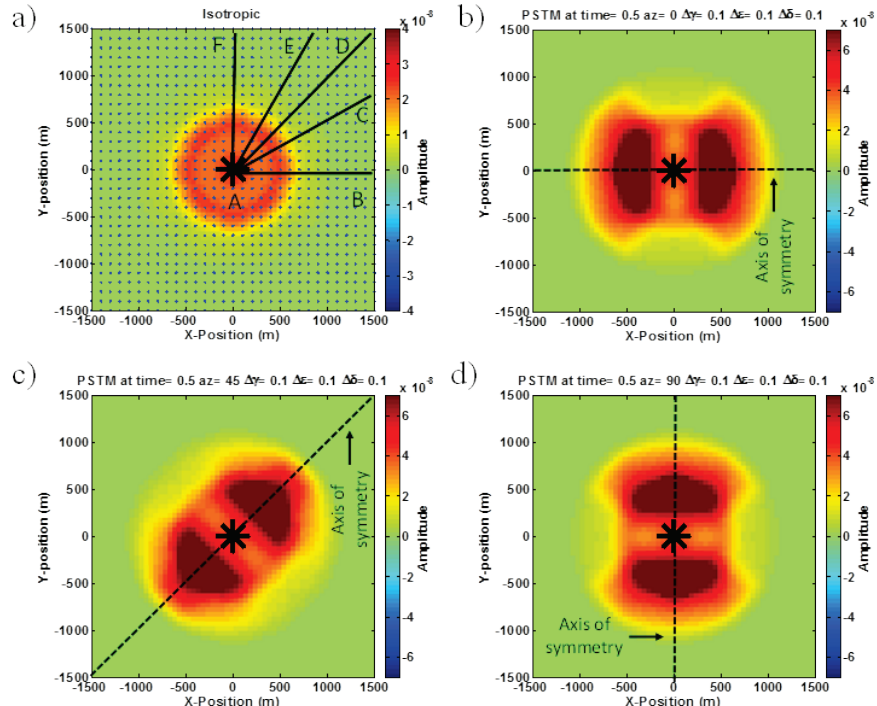


Figure 16: Evaluation of AVO/AZ formulation for different azimuth of axis of symmetry. The scenarios of Modeling#2 and Migration#2 are implemented for a) Isotropic media, b) HTI#1 media with axis of symmetry of  $\phi_{ref} = 0$ , c) HTI#2 media with axis of symmetry of  $\phi_{ref} = 45$  and d) HTI #3 media with axis of symmetry of  $\phi_{ref} = 90$ . The solid line in a) correspond to AVO/AZ curves sampling azimuth of  $0^\circ, 30^\circ, 45^\circ, 60^\circ$  and  $90^\circ$ .

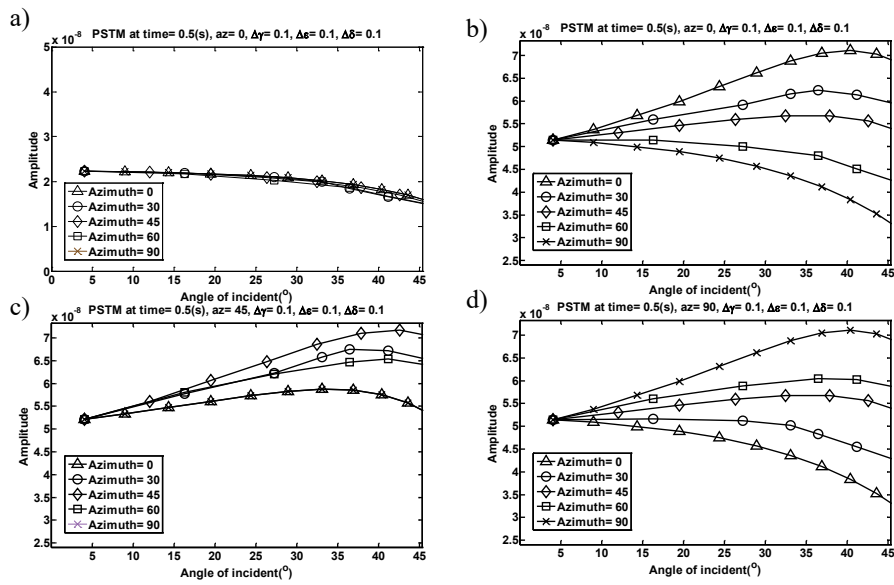


Figure 17: The AVO/AZ curves sampled from Figure 16. The scenarios for a) isotropic media, b) HTI#1 media with axis of symmetry of  $\phi_{ref} = 0$ , c) HTI#2 media with axis of symmetry of  $\phi_{ref} = 45$  and d) HTI#3 media with axis of symmetry of  $\phi_{ref} = 90$ .

The anisotropic parameters of HTI#4, HTI#5 and HTI#6 scenarios in Table 1 are shown in Figure 18. The acquisition parameters of Modeling/Migration#1 are used for simulation and migration. As expected by the theoretical evaluations in Figure 4, the trend of anisotropic parameter perturbation can be correlated to the seismic radiation patterns. In our acquisition configuration, the AVO/AZ curves show different patterns. The difference between the radiation patterns of anisotropic parameters are more visible in far offset. These examples show the importance of larger offset acquisition for estimation of anisotropic parameters.

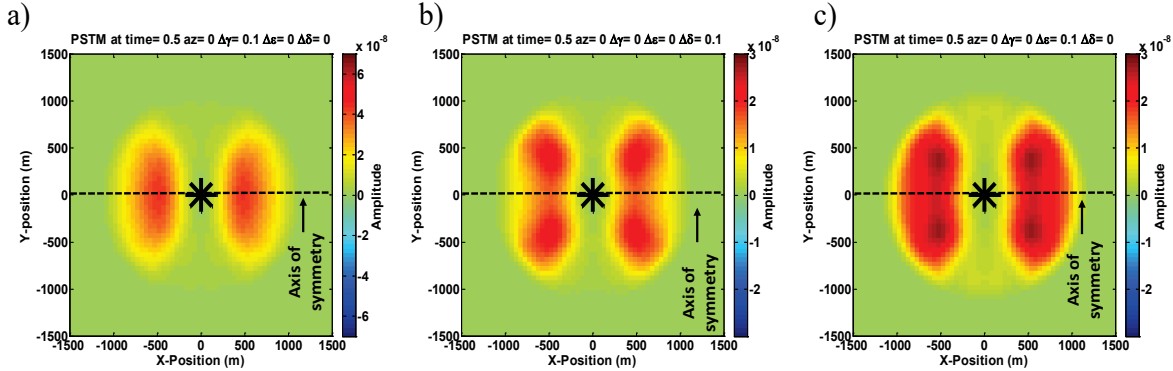


Figure 18: Evaluation of radiation pattern of anisotropic parameters for HTI media having  $\phi_{ref} = 0$ . The scenarios of Modeling#2 and Migration#2 are implemented for to obtain a) radiation pattern of  $\Delta\gamma$  in HTI#4 scenario, b) the radiation pattern of  $\Delta\delta$  in HTI#5 scenario and c) Radiation pattern of  $\Delta\epsilon$  in HTI#6 scenario.

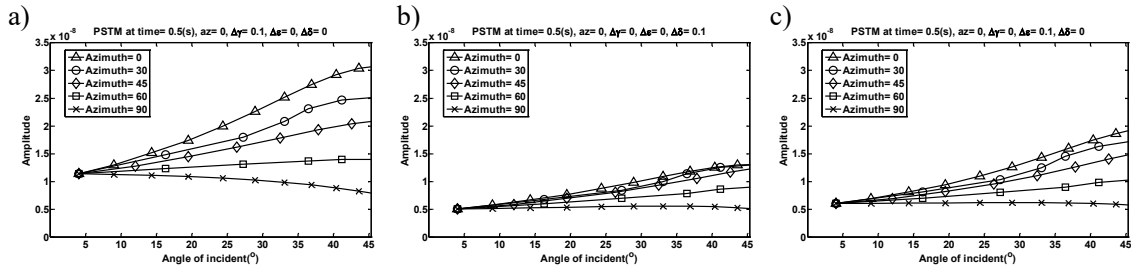


Figure 19: The AVO/AZ curves sampled from Figure 18. The scenarios for a) HTI#4 model, b) HTI#5 model, and c) HTI#6 model.

### VTI modeling and inversion

To study the radiation of anisotropic parameters in VTI medium, we implemented the model parameters of VTI#1, VTI#2 in Table 1. The acquisition parameters of Modeling/Migration#2 are used for simulation and migration. Figure 20 (a & b) shows the contribution of perturbation  $\Delta\epsilon$  and  $\Delta\delta$  respectively on the amplitude of the VTI medium. Their corresponding AVO/AZ curves are shown in Figure 21.

In analytical simulation, the radiation pattern of VTI (See e.g., Figure 5) and isotropic (See e.g., Figure 3a) are independent from azimuth. Ideally, it is expected to observe the similar azimuth independent property in numerical evaluations. Numerically, this pattern

of P-to-P waves AVO in VTI when combined with the limitation acquisition are not similar to isotropic models. As shown in Figure 21, the radiation patterns of VTI increase with offset while in isotropic model (see e.g., Figure 17a), maximum amplitude of AVO curve are in small angles. Similar acquisition artefacts are observed in AVO/AZ patterns of HTI models as seen in Figure 18.

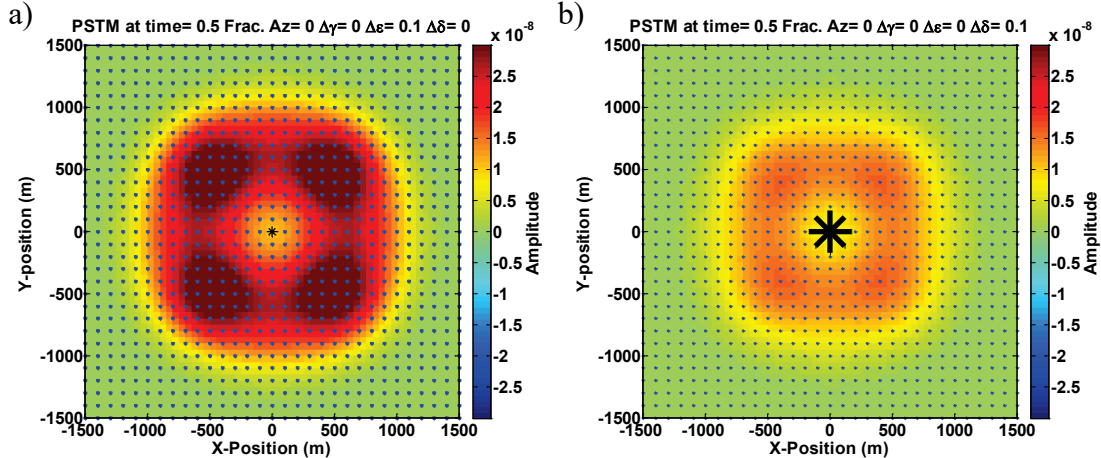


Figure 20: Evaluation of radiation pattern of anisotropic parameters for VTI media. The scenarios of Modeling#2 and Migration#2 are implemented for to obtain a) radiation pattern of  $\Delta\epsilon$  in VTI#1 scenario, b) the radiation pattern of  $\Delta\delta$  in VTI#2 scenario.

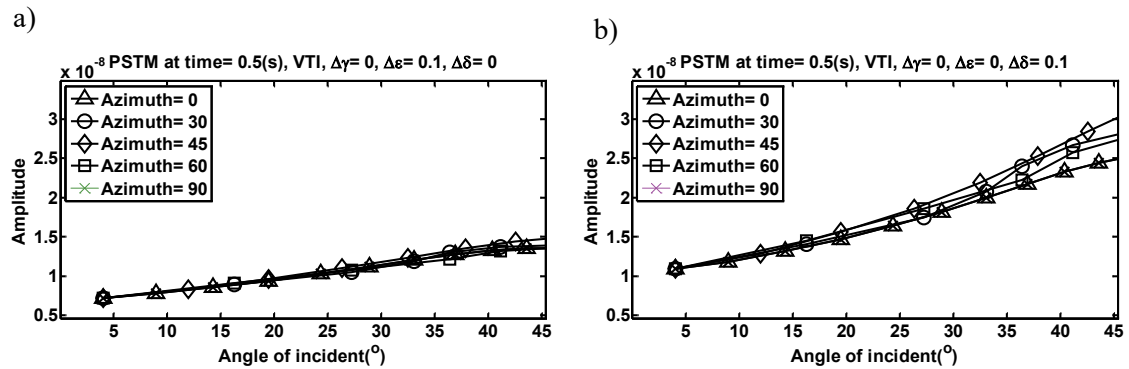


Figure 21: The AVO/AZ curves sampled from Figure 20. The scenarios for a) VTI#1 model, b) VTI #2 model. Please note that the amplitude curves of azimuth of  $\phi = 0$  overlapped on corresponding curve of  $\phi = 90$ .

## AVO/AZ INVERSE PROBLEM

Equations (11) and (20) can be written in the form of least square problem as,

$$Gm = R = \begin{bmatrix} A_{\theta_1\phi_1} & B_{\theta_1\phi_1} & C_{\theta_1\phi_1} & D_{\theta_1\phi_1} & E_{\theta_1\phi_1} & F_{\theta_1\phi_1} \\ \vdots & \vdots & \vdots & \vdots & \vdots & \vdots \\ A_{\theta_n\phi_1} & B_{\theta_n\phi_1} & C_{\theta_n\phi_1} & D_{\theta_n\phi_1} & E_{\theta_n\phi_1} & F_{\theta_n\phi_1} \\ \vdots & \vdots & \vdots & \vdots & \vdots & \vdots \\ \vdots & \vdots & \vdots & \vdots & \vdots & \vdots \\ A_{\theta_1\phi_m} & B_{\theta_1\phi_m} & C_{\theta_1\phi_m} & D_{\theta_1\phi_m} & E_{\theta_1\phi_m} & F_{\theta_1\phi_m} \\ \vdots & \vdots & \vdots & \vdots & \vdots & \vdots \\ A_{\theta_n\phi_m} & B_{\theta_n\phi_m} & C_{\theta_n\phi_m} & D_{\theta_n\phi_m} & E_{\theta_n\phi_m} & F_{\theta_n\phi_m} \end{bmatrix}_{nm \times 6} \times \begin{bmatrix} \Delta v_P / \bar{v}_P \\ \Delta Z / \bar{Z} \\ \Delta G / \bar{G} \\ \Delta \delta^{(V)} \\ \Delta \epsilon^{(V)} \\ \Delta \gamma \end{bmatrix}_{6 \times 1} = \begin{bmatrix} R_{\theta_1\phi_1} \\ \vdots \\ R_{\theta_n\phi_1} \\ \vdots \\ R_{\theta_1\phi_m} \\ \vdots \\ R_{\theta_n\phi_m} \end{bmatrix}_{nm \times 1} \quad (24)$$

where,  $\theta_n\phi_m$  corresponds to the reflectivity of a time slice of a target for an incident angle  $\theta_n$  and  $\phi_m$ . Theoretically, by reformulating the AVO/AZ we can estimate the perturbation model. As discussed in previous section, generally, the level of Signal to Noise Ratio (SNR) influences the result of inversion. In this study, we showed the effect of acquisition constrains on the AVO/AZ curves of migration results. As shown in previous section, constrains in data acquisition, (e.g., geophone spacing) effects the balance of amplitude of migration results.

We performed inversion on the three scenarios of seismic acquisitions and migrations in Figure 3d, Figure 13d and Figure 14d. The data obtained from a reference azimuth of symmetry axes  $\phi_0 = 0$  is considered for inversion of axes of symmetry  $\phi_{ref}$ . The result of AVO/AZ least square fitting is shown in Figure 22. The values for Figure 22a represent only the theoretical values that are modeled seismic data without any acquisition constrain. Slight deviation of amplitude of AVO/AZ curve from the theoretical trend is due to the sampling accuracy along AB, AC, AD, AE and AF direction of Figure 3. The least square fitting are plot by cross marking ("X") on the AVO/AZ curves. The quality of fitting in Figure 22b is less as compared with quality of Figure 22c. It is desired that the inverted values for the model parameters be consistent with HTI#3 scenario in Table 1. As shown in Table 3, the result of inversion in Figure 22b is not consistent with true values as it estimates negative perturbation for elastic parameter  $\Delta G / G$ .

In practical AVA/AZ implementation, due to uncertainty of direct detection of subsurface properties, the inverted parameters are calibrated with well logs and constrained with the values of anisotropic parameters obtained from the traveltome tomography in equations (22) and (23).

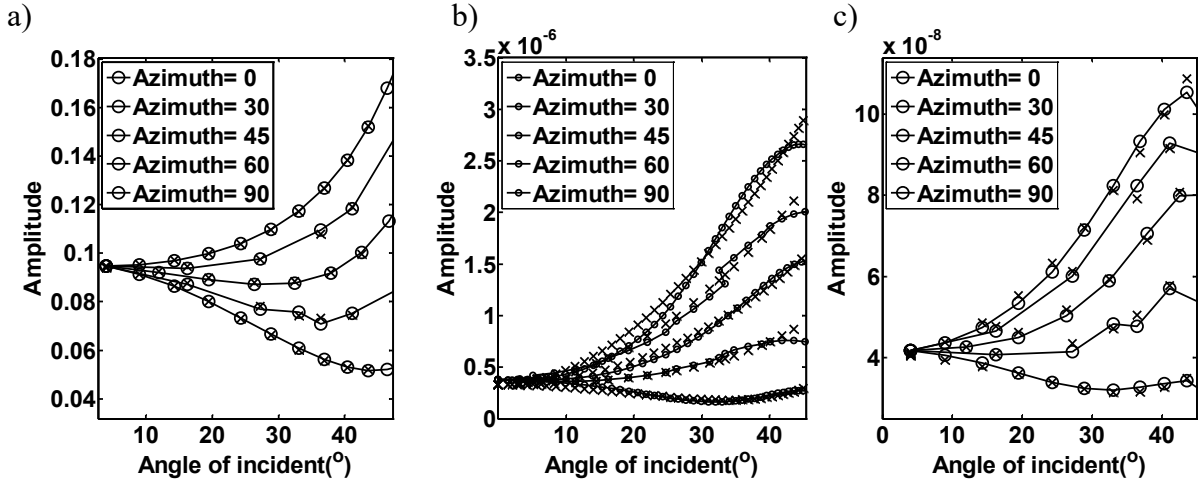


Figure 22: The AVO/AZ curves and the least square fitting values of a) Figure 3d, b) Figure 13d and c) Figure 14d. Figure 18 The scenario in a) HTI#4 model, b) HTI #5 model, c) HTI#6 model. The cross mark ‘x’ in each plot are the least square fitting of AVO/AZ curves.

Table 3: Anisotropic inversion results for Figure 23.

Inversion input	Figure (3d)	Figure (13d)	Figure (16d)
Reference data ( $\phi_0 = 0$ )	Figure (3b)	Figure (13b)	Figure (16b)
Scenario for HTI#3	Theoretical	Modeling/migration #1	Modeling/migration #2
$\frac{\Delta v_p}{v_p}$	0.107	0.100	0.1
$\frac{\Delta Z}{\bar{Z}}$	0.092	0.100	0.074
$\frac{\Delta G}{\bar{G}}$	0.082	-0.034	0.004
$\Delta \epsilon$	0.085	-0.055	-0.062
$\Delta \gamma$	0.121	0.264	0.069
$\Delta \delta$	-0.005	-0.025	0.253
$\phi_{ref}$	90°	90°	89°

## CONCLUSIONS

We analyzed an Kirchhoff based algorithm for multiparameter inversion for precritical reflection data within the framework of Full Waveform Inversion (FWI) methods. We coupled the Kirchhoff based forward modeling, migration and AVO/AZ analysis for waveform inversion of 3D anisotropic media. The approach is different from conventional FWI algorithms which use the imaging condition of extrapolated stress field for estimation of gradient function. In this technique, we relate the gradient function to the sensitivity of radiation pattern of scatterpoints to subsurface isotropic and anisotropic parameters.

To reduce the computational cost of inversion in 3D models, the linearized solution of the seismic reflection inverse problem is solved using standard PSTM and corresponding forward modeling. The AVO/AZ approximation of weak contrast anisotropic models and Double Square Root (DSR) equation for traveltime consideration of P-to-P are implemented during inversion. The procedure is analytically and numerically compared with the expected amplitudes of different acquisition patterns.

## ACKNOWLEDGEMENTS

The authors acknowledge the support from sponsors of CREWES and NSERC (Natural Science and Engineering Research Council of Canada) through the grant CRDPJ 461179-13. Thanks to Shahpoor Moradi for helpful discussions and suggestions.

## REFERENCES

- Aki, K., and Richards, P. G., 1980, Quantitative Seismology: Theory and Methods, W.H. Freeman and Company. Vol. 1.
- Cohen, J. .K. and Bleistein, N., 1979, Velocity inversion procedure of acoustic waves: *Geophysics*, 44, 1077-1087.
- Beylkin G., and Burridge R., 1990, Linearized inverse scattering problems in acoustics and elasticity, *Wave Motion*, 12, 15–52.
- Bleistein, N. (1987). On the imaging of reflectors in the earth. *Geophysics*, 52(7), 931–942.
- Gauthier, O., Virieux, J., and Tarantola, A., 1986, Two-dimensional nonlinear inversion of seismic waveforms: Numerical results: *Geophysics*, 51, 1387-1403.
- Grésillaud, A. and Cara, M. 1996, Anisotropy and P-wave tomography: a new approach for inverting teleseismic data from a dense array of stations. *Geophysical Journal International*, 126: 77–91.
- Jaramillo, H. and Bleistein, N. (1999). "The link of Kirchhoff migration and demigration to Kirchhoff and Born modeling. *Geophysics*, 64(6), 1793–1805.
- Morse, P. M., and Feshbach, H., 1953. Methods of theoretical physics: McGraw-Hill Book Co. Vol. 2.
- Khani H., Bancroft J. C., and Margrave G. F., 2012, Full waveform inversion algorithm using Common Scatter Point (CSP) gathers: SEG Expanded Abstracts.
- Khani H., Bancroft, J. C., and Lunen v. E., 2016. Iterative multiparameter waveform inversion of precritical reflection data using prestack time Kirchhoff approximation *Geophysics*, 81, R15-R27.
- Kroode T. F., 2012: A wave-equation-based Kirchhoff operator: *Inverse Problems*, 28(11), 115013.
- Moradi, S. & Innanen K. A., 2015. Scattering of homogeneous and inhomogeneous seismic waves in low-loss viscoelastic media, *Geophys. J. Int.*, 202, 1722-1732.
- Musgrave, M. J. P., 1970, Crystal acoustic: Holden Day.
- Rüger, A., and I. Tsvankin, 1997, Using AVO for fracture detection: Analytic basis and practical solutions: *The Leading Edge*, v. 16/10, p.1429–1434.
- Rüger, A., 2001, Reflection coefficients and azimuthal avo analysis in anisotropic media: Geophysical Monograph Series.
- Shaw, R. K., and M. K. Sen, 2004, Born integral, stationary phase, and linearized reflection coefficients in anisotropic media: *Geophysical Journal International*, 158, 225–238.
- Tarantola, A., 1984, Inversion of seismic reflection data in the acoustic approximation: *Geophysics*, 49,1259–1266.
- Tsvankin, I., 1997, Anisotropic parameters and P-wave velocity for orthorhombic media: *Geophysics*, 62, 1292–1309.
- Tsvankin, I., 1997b, Reflection moveout and parameter estimation for horizontal transverse isotropy: *Geophysics*, 62, 614–629.
- Ursin, B., and Tygel, M., 1997: Reciprocal volume and surface scattering integrals for anisotropic elastic media, *Wave Motion*, 26, pp. 31-42.
- Virieux, A., and Operto, S., 2009, An overview of full-waveform inversion in exploration geophysics: *Geophysics*, 74, WCC1–WCC26.